Pattern Formation in a 4-Ring Reaction-Diffusion Network with Heterogeneity
Electronic Supplement

Ian Hunter,[1, *] Michael M. Norton,[2, *] Bolun Chen,[3, 4] Chris Simonetti,[1]
Maria Eleni Moustaka,[1] Jonathan Touboul,[3, 5] and Seth Fraden[1, †]

[1]*Brandeis University Physics, Waltham MA, 02453 USA*
[2]*Center for Neural Engineering, Department of Engineering Science and Mechanics,*
The Pennsylvania State University, University Park, PA 16802 USA
[3]*Brandeis University Volen National Center for Complex Systems, Waltham MA, 02453 USA*
[4]*Department of Physics Boston University, Boston MA, 02215 USA*
[5]*Brandeis University Mathematics Department*
(Dated: February 2, 2022)

* These two authors contributed equally

† To whom correspondence should be addressed:fraden@brandeis.edu

SI. MOVIES

- Movie S1: Video of an experimental network converging to the Trot attractor: Initially three reactors flash at a similar times, with the fourth flashing out of phase relative to them. As time goes on the system converges to a nearly ideal realization of the Trot state. The raw video of the experiment is shown alongside a space-time plot of the video and the calculated phase differences between reactors 1 and 2, 2 and 3, and 3 and 4. The phase differences are denoted $\theta_{ij} \equiv \phi_i - \phi_j$.

- Movie S2: Video of an experimental network in the Pace attractor: The experiment starts in a Pace pattern and proceeds to stay in it during the rest of the experiment. The raw video of the experiment is shown alongside a space-time plot of the video and the calculated phase differences between reactors 1 and 2, 2 and 3, and 3 and 4.

- Movie S3: Video of an experimental network in the Pronk attractor: The experiment starts in a Pronk state and proceeds to stay in it the during rest of the experiment. The raw video of the experiment is shown alongside a space-time plot of the video and the calculated phase differences between reactors 1 and 2, 2 and 3, and 3 and 4.

- Movie S4: Video of an experimental network in an unideal Trot steady-state: The experiment starts and stays in a state in which flashing is initiated at the top left, and proceeds to the bottom right reactor in a Z-pattern. Although it is visually unlike the idealized Trot state, it is at the tail of an distribution of steady-states centered about Trot. The raw video of the experiment is shown alongside a space-time plot of the video and the calculated phase differences between reactors 1 and 2, 2 and 3, and 3 and 4.

- Movie S5: Video of rotation about 3D plot in manuscript Fig. 5(a) which shows the state-space of the theoretical model.

- Movie S6: Video of rotation about a 3D plot of the same state-space as Fig. 5(a) except with experimental data. Since many experiments start near steady-state, some trajectories are short.

- Movie S7: Video of rotation about 3D plot in manuscript Fig. 5(b) which shows basins of attraction of the theoretical model and experiments.

- Movie S8: Annotated video of experiment converging from Pronk to Pace Fig. 6(a). The raw video of the experiment is shown alongside a space-time plot of the video and evolution of the phase differences between reactors moving through the state-space of the network. As during this experiment the 2nd and 3rd reactor oscillate in-phase, only the 2D slice of the state-space in which the trajectory is confined to, $\theta_{32} = 0$, is shown. Within this view of state-space the 1D H/K predicted invariant manifold (D_1^s, D_1^s) is shown and is colored by its maximum transverse eigenvalue, as in the manuscript Fig. 6a)(c). The experimental trajectory noisily moves about Pronk before transitioning to Pace directly along the invariant manifold.

- Movie S9: Annotated video of experiment converging from Pronk to Trot Fig. 6(b). The raw video of the experiment is shown alongside a space-time plot of the video and evolution of the phase differences between reactors moving through the state-space of the network. As during this experiment the 1st and 3rd reactor oscillate in-phase, only the 2D slice of the state-space in which the trajectory is confined to, $\theta_{32} = -\theta_{21}$ where $\phi_1 = \phi_3$, is shown. Within this view of state-space the 2D H/K predicted invariant manifold (D_1^p, D_1^p) is shown and is colored by its maximum transverse eigenvalue, as in the manuscript Fig. 6(b)(c). The experimental trajectory starts near Pronk before transitioning to Trot, following the in-plane velocity field of the 2D the invariant manifold.

- Movie S10: Video of rotation about 3D plot in manuscript Fig. 6(c) which shows theoretical stability of invariant manifolds. The video starts from the perspective of the Fig. 6(c), then rotates about it to help readers understand the structure of the invariant manifold stability.

- Movie S11: Video of rotation about 3D plot in manuscript Fig. 4(a) which shows the steady-states of experiments. The video starts from the perspective of the Fig. 4(a), then rotates about it to help readers understand the 3D structure of the steady-states in the state-space of the experiments. It can be seen clearly that the Other states are distributed anisotropically about Trot, such that they are more widely spread across a plane spanned by the two linear, orange invariant manifolds, $(D_1^s, 1)$.

- Movie S12: Video of rotation about 3D plot in manuscript Fig. 8(a) which shows the steady-states of heterogeneous simulations. The video starts from the perspective of the Fig. 5(b), then rotates about it to help readers understand the 3D structure of the steady-states in the state-space of the heterogeneous model.
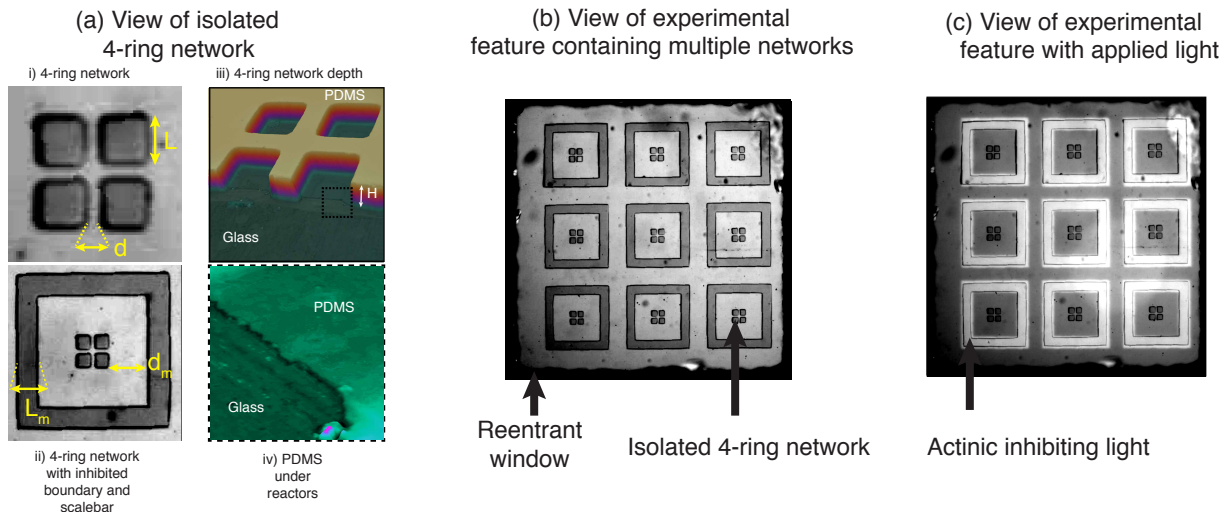
SII.   ADDITIONAL EXPERIMENTAL DETAILS

(a) View of isolated 4-ring network

i) 4-ring network

iii) 4-ring network depth

ii) 4-ring network with inhibited boundary and scalebar

iv) PDMS under reactors

(b) View of experimental feature containing multiple networks

Reentrant window   Isolated 4-ring network

(c) View of experimental feature with applied light

Actinic inhibiting light

FIG. S1. **(a)** i) A single network of four coupled BZ reactors. The side lengths, L, of the reactors are 62 µm, side-to-side distances, d, between reactors are 26 µm. ii) The distance between a reactor and the inner surface of the inhibited boundary, d_m, was 130 or 190 µm. The thickness of the inhibited boundary, L_m, was 100 µm. iii) 50X magnification profilometer image of cut microfluidic reactor network showing the out of plane height H of the reactors is 30 µm and iv) 100X magnification profilometer image of cut microfluidic reactor network showing there is below 2 µm of PDMS between the bottom of the reactors and the glass below it. **(b)** View of running experiment with nine parallelized 4-node ring networks running simultaneously. The reentrant window is a piece of glass used to seal the BZ into the lattice. The black region along the borders, outside the reentrant window, is filled with oscillatory BZ reaction. **(c)** View of same experiment except with actinic, inhibiting light selectively patterned onto the orders.

.

SIII.   EXPLANATION OF BEST FIT MODEL

A.   Fitting to experiments/choice of free parameters

The best fit model corresponds to substantially weaker than expected diffusive coupling. The diffusive coupling rate predicted by quasi-static diffusion between rectangular reactors is given by

$$k_{\text{ideal}} = \frac{PD}{Ld} \tag{S1}$$

where P is the partition coefficient, D the diffusion coefficient, L the side length of the reactors, and d is the distance between reactors. In our case $D = 10^{-9}[\text{m}^2\,\text{s}^{-1}]$, $P = 2.5[1]$, $L = 62[\text{µm}]$, and $d = 26[\text{µm}]$. Thus, the idealized coupling rate is $k_{\text{ideal}} = 2.[\text{s}^{-1}]$.

The best fit value of k (manuscript Table VI) is two orders of magnitude below k_{ideal}. As Br_2 is known to partition into and react with oil and PDMS, more PDMS would cause a reduction in inter-reactor coupling. We hypothesize that this is the cause of the discrepancy.

Since the coupling rate equation Eqn. S1 is composed of geometric parameters L and d that are precisely prescribed by the photolithographic process, the discrepancy is isolated to the product of the two less certainly known material properties P and D. We can therefore consider our fits as a measurement of the product PD. Given the best fit $k = 2. \times 10^{-2}[\text{s}^{-1}]$, $PD = 3. \times 10^{1}[\text{µm}^2\,\text{s}^{-1}]$.

The necessity of excitatory coupling is due to observation of robust in-phase synchronization during experiments. Without excitatory coupling ($k_e = 0$), the best fits to experiments with initial conditions that converged to Pronk and Bound were inaccurate as they would always converge to Trot. Although with no excitatory coupling, $k_e = 0$, the phase model has Pronk and Bound as attractors, the basins of attraction of Pronk and Bound are much smaller than
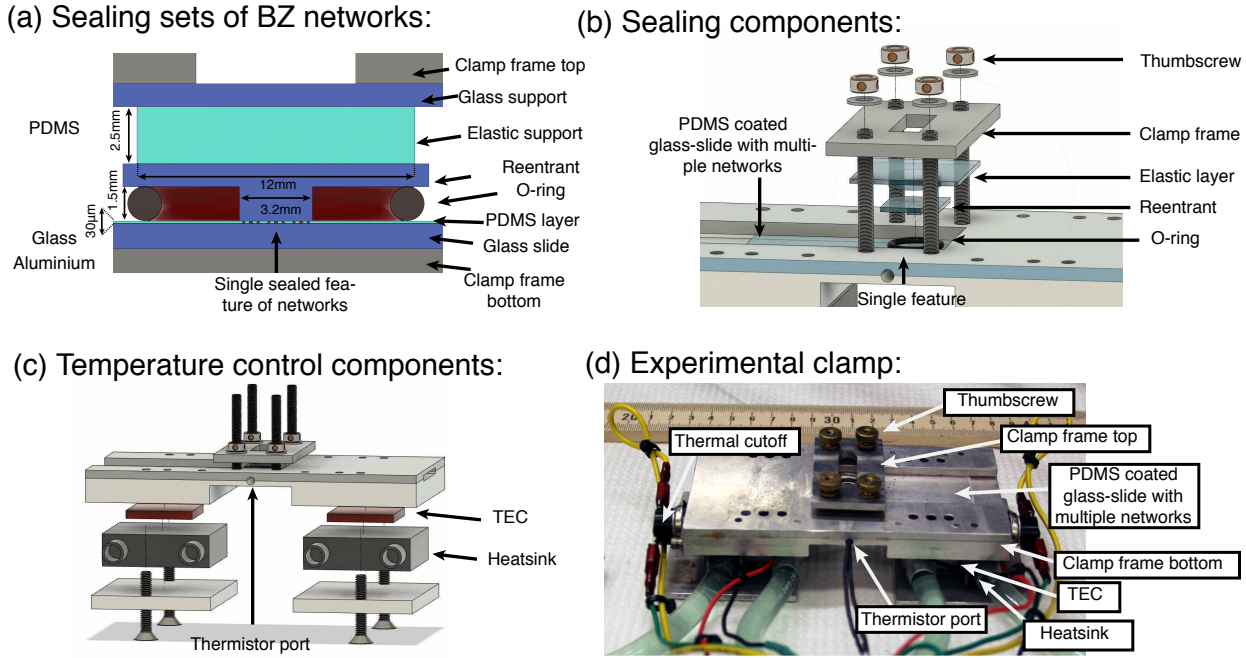
FIG. S2. Temperature controlled BZ clamp. **(a)** CAD diagram of sealing of a set, or feature, of BZ networks. The networks are sealed above and below by glass. A volume of extraneous BZ is also sealed, however is irrelevant to the dynamics of the network. Sealing is achieved by gradual adjustment of fine-threaded (6-80) thumbscrews. These apply force via a metal clamp frame, and softened by an 2.5mm thick layer of PDMS. **(b)** CAD diagram rendering of sealing components of the clamp. **(c)** CAD diagram of the temperature controlling elements of the clamp. Temperature measurement occurs through a thermistor. The clamp is heated and cooled using 2 thermoelectric cooler (TEC) peltier elements placed symmetrically about the sample. Feedback between them is performed using an Arduino's standard PID libraries. **(d)** Photograph of temperature-controlled clamp containing a sealed network. All components of the clamp are clearly visible except the TECs, elastic layer, reentrant window, and o-ring. Unlike in simplified diagrams (a),(b), and (c), three other necessary components of the clamp are pictured: wiring, water circulating tubes connected to the heat sinks, and thermal cutoffs. The wiring connects the peltier TECs and thermistor to the controlling Arduino. The tubes circulate water through the heat sinks and cools the water down using fan radiators. The thermal cutoffs in series with the TECs short-circuit reversibly if the clamp become hot, above 50 °C, by some error. A meter stick is shown for reference (units of cm).

experimentally observed. Allowing finite excitatory coupling, specifically $k_e = 0.05$, achieved good fits to experimental data.

B. Best fit model: All steady-states

In the main manuscript, we focus on the H/K predicted attractors. Additionally, we attempted to find all remaining steady-states $\boldsymbol{\theta}^\dagger$, such that $\boldsymbol{\Psi}(\boldsymbol{\theta}^\dagger) = \mathbf{0}$, of the homogeneous model $\boldsymbol{\Delta\omega} = \mathbf{0}$. This was achieved by dividing state-space into a 100x50x50 grid and initializing a Newton-Raphson search at each grid point. The result of the search $\boldsymbol{\theta}_n^\dagger$ was considered a valid steady-state if $|\boldsymbol{\Psi}(\boldsymbol{\theta}_n^\dagger)|^2 < 1 \times 10^{-16}$. The identified steady-states are shown as space-time plots with their maximum eigenvalue and topological index in Fig. SI and as colored points in the state-space in Fig. S6. The state-space contains 168 steady-states Fig. SI; 10 of which are attractors or repellers while the remaining 158 are all saddle steady-states. We believe this method may have discovered all steady-states since all their topological indices sum to 0, the Euler characteristic of the state-space [Sec. SV]. Regardless of whether we found all steady-states, it does show: (1) The unique stable steady-states are the H/K point invariant manifolds and (2) the state-space possess a wealth of unstable, saddle steady-states. This method was too slow to be used to efficiently calculate the steady-states of the model with heterogeneity.

(a) Ray diagram of programmable illumination microscope

(b) Programmable illumation example

Projected image

CCD view

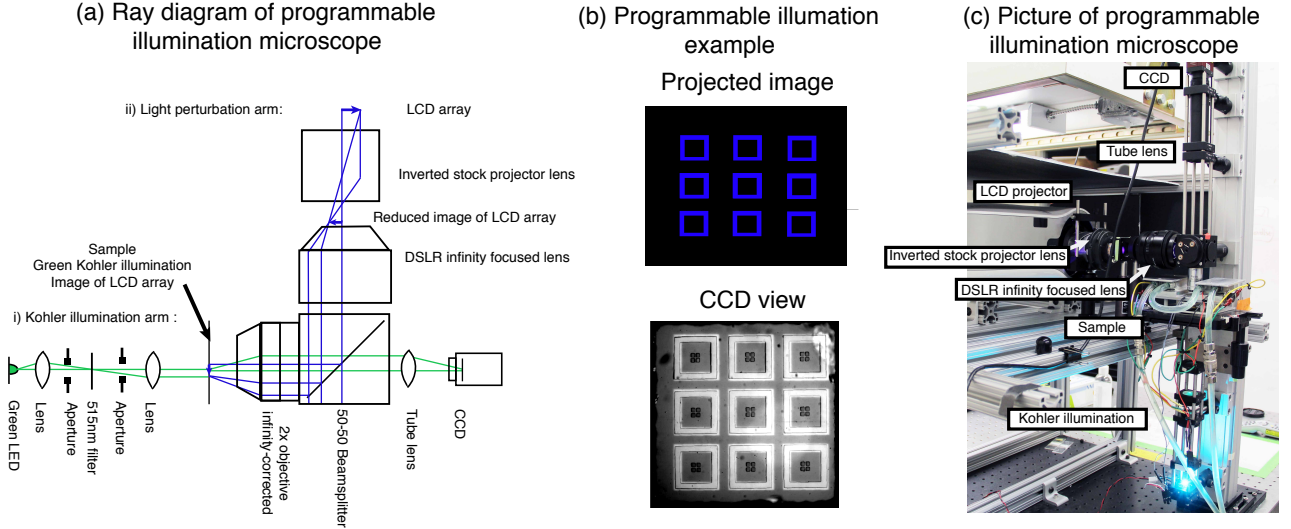**(c) Picture of programmable illumination microscope**

FIG. S3. **(a)** Ray diagram of a both i) microscopy imaging of BZ networks and ii) their spatiotemporal perturbation with light. i) Imaging of the networks functions through 515nm green transmission illumination, ii) Spatiotemporal perturbation is achieved by imaging a commercial liquid-crystal display (LCD) projector's LCD array set to project pure blue light onto the sample. The blue light efficiently excites the photo-sensitive, oscillation-inhibiting catalyst. **(b)** Example of how spatiotemporal light patterning is achieved and its quality. Images are projected onto the sample by sending images to a VGA/HDMI port connected to the projector, an example is labeled 'Projected image'. This can be done through powerpoint, however we use MATLAB. This image then hits the sample, homogeneous and in crisp focus, shown in 'CCD view'. **(c)** Picture of full experimental apparatus, including a clamped, temperature-controlled sample. Overhead light shown in picture not on during experiments.

SIV. LINEAR STABILITY ANALYSIS OF 2D AND 1D INVARIANT MANIFOLDS

A. Example: computing the maximum transverse eigenvalue of an invariant manifold

Following the algorithm present in Appendix E for the invariant manifold (D_1^p, D_1^p):

1. We choose the invariant manifold (D_1^p, D_1^p). It is a 2D manifold in the 3D state-space of the 4 ring network.

2. The invariant manifold (D_1^p, D_1^p) is parameterized by $\boldsymbol{\theta} = (\eta_1, -\eta_1, \eta_2)$, manuscript Table II. The set of tangent vectors which span it are $T = \{\sqrt{2}^{-1}(1, -1, 0), (0, 0, 1)\}$. The one vector normal, which we put in our set of possible normal vectors $N = \{2^{-\frac{1}{2}}(1, 1, 0)\}$.

3. We now compute the unitary transformation matrix P. In the case of the 4 ring's invariant manifold this is very simple:

$$P = [\mathbf{t}_1 \mathbf{t}_2 \mathbf{n}_1]^T = \frac{1}{\sqrt{2}} \begin{bmatrix} 1 & -1 & 0 \\ 0 & 0 & \sqrt{2} \\ 1 & 1 & 0 \end{bmatrix}$$

4. For our particular 4 ring network the Jacobian J is given by:

$$J(\boldsymbol{\theta}) = -k \begin{bmatrix} [H'(\theta_{21})+H'(-\theta_{21})+H'(\theta_{43}+\theta_{32}+\theta_{21})] & [-H'(\theta_{32})+H'(\theta_{43}+\theta_{32}+\theta_{21})] & H'(\theta_{43}+\theta_{32}+\theta_{21}) \\ -H'(-\theta_{21}) & [H'(\theta_{32})+H'(-\theta_{32})] & -H'(\theta_{43}) \\ H'(-(\theta_{43}+\theta_{32}+\theta_{21})) & [H'(-(\theta_{43}+\theta_{32}+\theta_{21}))-H'(-\theta_{32})] & [H'(\theta_{43})+H'(-\theta_{43})+H'(-(\theta_{43}+\theta_{32}+\theta_{21}))] \end{bmatrix},$$
(S2)

where $H'(x) = \frac{dH(\chi)}{d\chi}|_{\chi=x}$. Note that since we numerically computed H, H' is computed numerically as well.

5. We compute $J' = PJP^{-1}$.

$$J' = \begin{bmatrix} -2H'(-\theta_{21}) - H'(\theta_{21}) & -2H'(\theta_{43}) & -H'(\theta_{43}) \\ -\frac{1}{2}H'(\theta_{21}) & -2H'(-\theta_{43}) - H'(\theta_{43}) & \frac{1}{2}(H'(\theta_{21}) - 2H'(-\theta_{43})) \\ 0 & 0 & -H'(\theta_{21}) - H'(\theta_{43}) \end{bmatrix}$$
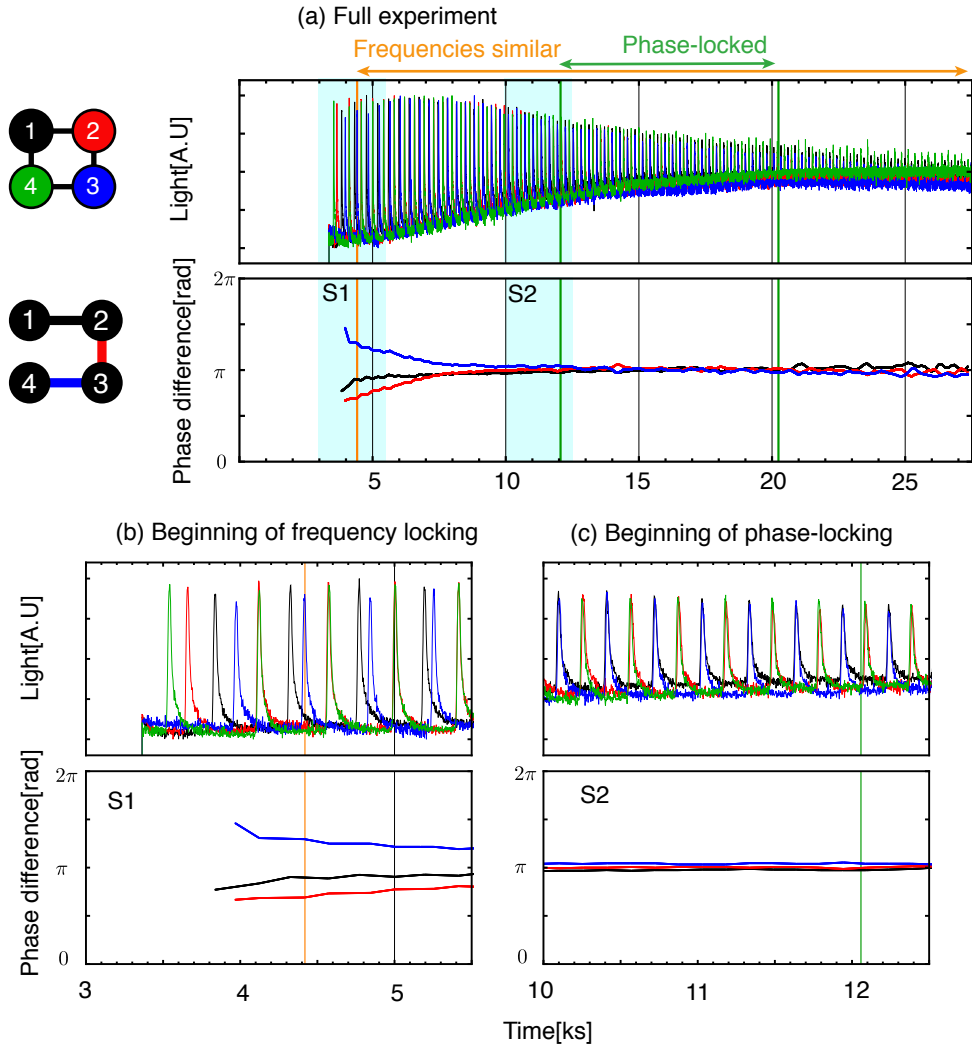
FIG. S4. **(a)** View of a single 4 reactor network over time during an entire experiment. The top plot is of light transmitted through the reactors. It is normalized from the raw intensity measured as an average of a square of pixels inside a reactor [Fig. S1(b)]. Specifically if the raw signal was $I(t)$, with a maximum value during the experiment was I_{max} and a minimum at I_{min}, the normalized intensity was $(I(t) - I_{min})/(I_{max} - I_{min})$. As time goes on, the amplitude of the light peaks goes downwards, while the baseline increases. The lower panel tracks the phase differences between the reactors versus time. Eventually the reactors reach a phase-locked steady-state in which all reactors are firing antiphase their two neighbors. Since the phase differences between the reactors are never perfectly stationary, we use a specific threshold for when phase differences evolve slowly enough to be considered phase-locked in Appendix B. At about 20,000s the experiment ceases to be considered phase-locked as its phase differences become noisy. **(b)** An inset of early times in the experiment. Note that the frequencies and amplitudes of oscillation of the reactors are initially not the same. For example, the interval between the first two spikes of reactors 2(red) and 4(green) are different, and the amplitudes of 3(blue) and 4(green) are different. However, at about 4,400s the reactors possess similar frequencies by the threshold in Appendix A Protocol. **(c)** An inset of later times in the experiment. Note that the frequencies and amplitudes of oscillation of the reactors are very similar. At the green line marking 12,050s, the threshold for phase-locking is met.

6. We extract the 'block' of dynamics corresponding to perturbations in the only normal direction

$$[-H'(\theta_{21}) - H'(\theta_{43})]$$

7. In general, this extracted block will not be 1×1 and the max transverse eigenvalue will be its max real eigenvalue. Since the matrix is 1×1, the value itself is the MTE. We conclude that a infinitesimally small perturbation
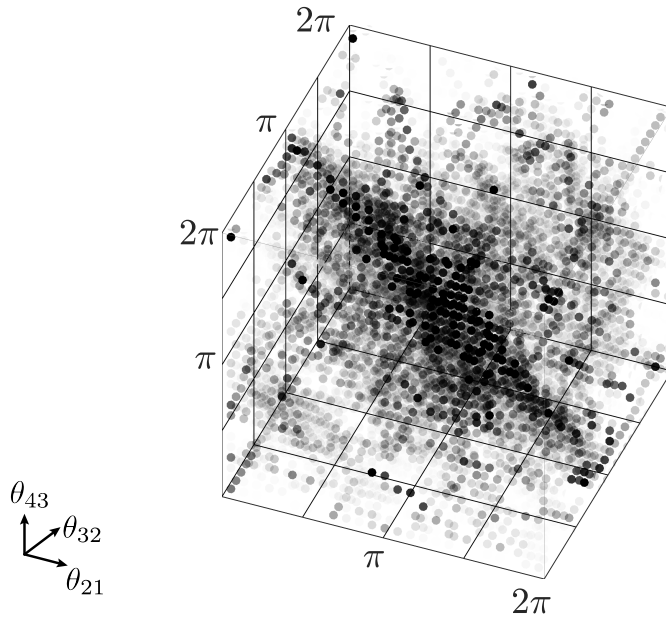
FIG. S5. Histogram of all phase differences observed during experiments categorized as phase-slipping and not discussed in main paper. Each dot's opacity is proportional to the number of states observed within a cube centered about the point. The data fills much of the cube, although more states are about Trot and Bound. The fact the distribution does not also include a thick band connecting Trot and Pace, as it does Trot and Bound is surprising. This does open the possibility of a bias in the up-down versus left-right setup of our experiment Fig. S3. We hypothesize this is due to a systematic asymmetry in applied light, temperature, or sealing.

normal the (D_1^p, D_1^p) invariant manifold δn will evolve according to the equation

$$\frac{d}{dt} \delta n = \left[-H'(\theta_{21}(t)) - H'(\theta_{43}(t)) \right] \delta n$$

.

B. Transverse eigenvalues for weakly coupled 4-ring networks

We now present the transverse eigen values for a 4 ring network of phase oscillators for a generic phase model with interaction function H. With the exception of the linear invariant H/K manifold $(Z_2, 1)$, all of them are simple. We used the algorithm proposed in the previous section on each invariant manifold to transform this Jacobian J to identify the dynamics transverse to the manifold in J'. The result of these calculations are shown in Table SII is the block of J' corresponding to components normal or transverse the each invariant manifold.

Space–time plot	LE[1/s]	Type	$\{\theta_{21},\theta_{32},\theta_{43},\theta_{14}\}$	Index	Repeats
	−0.0012	Attractor	{0.5, 0.5, 0.5, 0.5}	−1	1
	−0.00056	Attractor	{0.25, 0.25, 0.25, 0.25}	−1	2
	−0.00018	Attractor	{0.5, 0., 0.5, 0.}	−1	2
	−0.00018	Attractor	{0., 0., 0., 0.}	−1	1
	0.0014	Saddle	{0.3, 0.26, 0.12, 0.32}	1	8
	0.0014	Saddle	{0.26, 0.3, 0.32, 0.12}	1	8
	0.0059	Saddle	{0.1, 0.37, 0.44, 0.09}	−1	8
	0.0059	Saddle	{0.37, 0.1, 0.08, 0.45}	−1	8
	0.0059	Saddle	{0.1, 0.08, 0.44, 0.38}	−1	8
	0.0059	Saddle	{0.08, 0.44, 0.37, 0.11}	−1	8
	0.0059	Saddle	{0.37, 0.44, 0.08, 0.11}	−1	8
	0.0059	Saddle	{0.44, 0.08, 0.1, 0.38}	−1	8
	0.0059	Saddle	{0.08, 0.1, 0.37, 0.45}	−1	8
	0.0059	Saddle	{0.44, 0.37, 0.1, 0.09}	−1	8
	0.0075	Saddle	{0.42, 0.08, 0.42, 0.08}	−1	4
	0.008	Saddle	{0.5, 0.03, 0.55, 0.92}	1	8
	0.008	Saddle	{0.45, 0.07, 0.5, 0.98}	1	8
	0.008	Saddle	{0.03, 0.55, 0.93, 0.49}	1	8
	0.008	Saddle	{0.07, 0.5, 0.97, 0.46}	1	8
	0.008	Saddle	{0.55, 0.03, 0.5, 0.92}	1	8
	0.008	Saddle	{0.5, 0.07, 0.45, 0.98}	1	8
	0.0085	Saddle	{0., 0.07, 0., 0.93}	−1	4
	0.0085	Saddle	{0.07, 0.5, 0.93, 0.5}	−1	4
	0.015	Saddle	{0.08, 0.43, 0.57, 0.92}	1	4
	0.015	Saddle	{0.43, 0.08, 0.92, 0.57}	1	4
	0.017	Repellor	{0.93, 0.07, 0.07, 0.93}	1	4
	0.017	Saddle	{0.93, 0.07, 0.01, 0.99}	1	4
	0.017	Saddle	{0.01, 0.07, 0.93, 0.99}	1	4
	0.017	Saddle	{0.07, 0.93, 0.07, 0.93}	−1	2

TABLE SI. A list of numerically identified symmetrically unique steady-states of the best fit model of the homogeneous 4 ring network. For each state we computed: (first column) An example of the space-time plot of the state, (second) The maximum eigenvalue of the dynamics linearized about the steady-state with units [s^{-1}], indicating the exponential rate at which nearby trajectory collapse to, if $\lambda < 0$, or diverge from, if $\lambda > 0$, the steady-state, (third) whether or not the state is an Attractor, Repeller, or a Saddle, (forth) the phase differences of the steady-state divided by 2π, i.e. as fractions of a period, (fifth) the topological index of the steady-state, and (sixth) the number of distinct states in state-space equivalent the unique state on the left. To be precise the number of distinct states is equal to the number of 4-tuples of phase differences $(\theta_{21}, \theta_{32}, \theta_{43}, \theta_{14})$ generated by operating on the state on the left by every element of the symmetry group D_4 and then modulo 2π.

Terms for $(Z_2, 1)$ invariant manifold:
$$J'(z2,1)_{11} = \tfrac{1}{3}(2H'(\pi + \theta_{21}) + H'(-\pi + \theta_{21}) - 3H'(\theta_{21}) - 3H'(-\theta_{21}) - H'(-\theta_{21} + \pi)) - 2H'(-\theta_{21} - \pi))$$
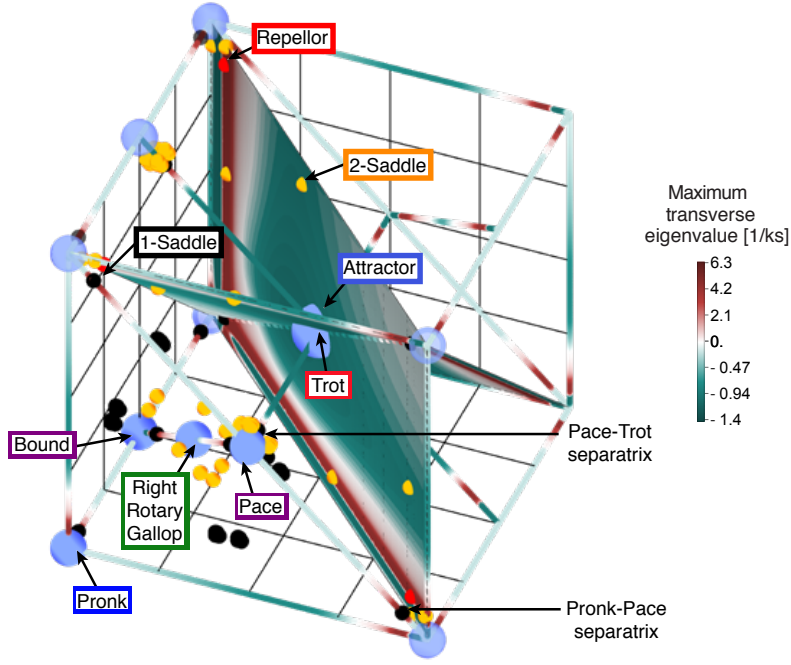
FIG. S6. All steady-states of best fit model without heterogeneity which are in the half state-space $\theta_{32} > 2\pi - \theta_{21}$, colored by type: Blue are Attractors with index=-1, Orange are saddles with 2 attracting direction saddles and thus index=1, Black are saddles with 1 attracting direction and thus with index=-1, Red Repellers with index=1. Points are faint if they are a periodic instance of another steady-state. The unstable steady-stats which form the separatrices between Pronk and Pace, and Pace and Trot are also marked.

TABLE SII. Decoupled transverse linear dynamics of invariant manifolds universal to four-rings. $H'(x) = \frac{dH(\chi)}{d\chi}|\chi = x$. The maximum transverse eigenvalue of a given invariant manifold is the maximum real component of the eigenvalue of the associated matrix.

H	K	Transformed Jacobian J' normal dynamics block
		Linear invariant manifolds:
D_1^s	D_1^s	$-\begin{bmatrix} 2H'(0) + H'(-\theta_{32}) & H'(-\theta_{32}) \\ H'(\theta_{32}) & 2H'(0) + H'(\theta_{32}) \end{bmatrix}$
D_1^s	1	$-\begin{bmatrix} 2H'(\pi) + H'(-\theta_{32}) & H'(-\theta_{32}) \\ H'(\theta_{32}) & 2H'(\pi) + H'(\theta32) \end{bmatrix}$
Z_2	1	$\begin{bmatrix} J'(z2,1)_{11} & J'(z2,1)_{12} \\ J'(z2,1)_{21} & J'(z2,1)_{22} \end{bmatrix}$
		Planar invariant manifolds:
D_1^p	D_1^p	$-H'(\theta_{21}) - H'(\theta_{43})$

$J'(z2,1)_{12} = -\frac{2}{3}(-2H'(\pi - \theta_{21}) - H'(-\pi + \theta_{21}) + H'(\pi - \theta_{21}) + 2H'(-\pi - \theta_{21}))$
$J'(z2,1)_{21} = \frac{1}{3}(-2H'(\pi + \theta_{21}) - H'(-\pi + \theta_{21}) + 3H'(\theta_{21}))$
$J'(z2,1)_{22} = -\frac{2}{3}(2H'(\pi + \theta_{21}) + H'(-\pi + \theta_{21}))$

C. Transverse stability of invariant manifolds: Kuramoto model compared to BZ phase model

Having both parameterized the invariant manifolds guaranteed by symmetry (manuscript Table II) and provided expressions for the MTE of these invariant manifolds for the 4 ring network (Table SII), we now compare the stability of the manifolds for Kuramoto and best fit BZ-in-PDMS interaction functions. Fig. S7 shows the MTE as heatmaps along invariant manifolds for (A) the Kuramoto 4 ring ($H(\chi) = -\sin(\chi)$) and (B) the BZ best fit model [manuscript Table VI and Fig. 2].

We observe that the two 4 node networks are qualitatively different. The Kuramoto model's invariant manifolds
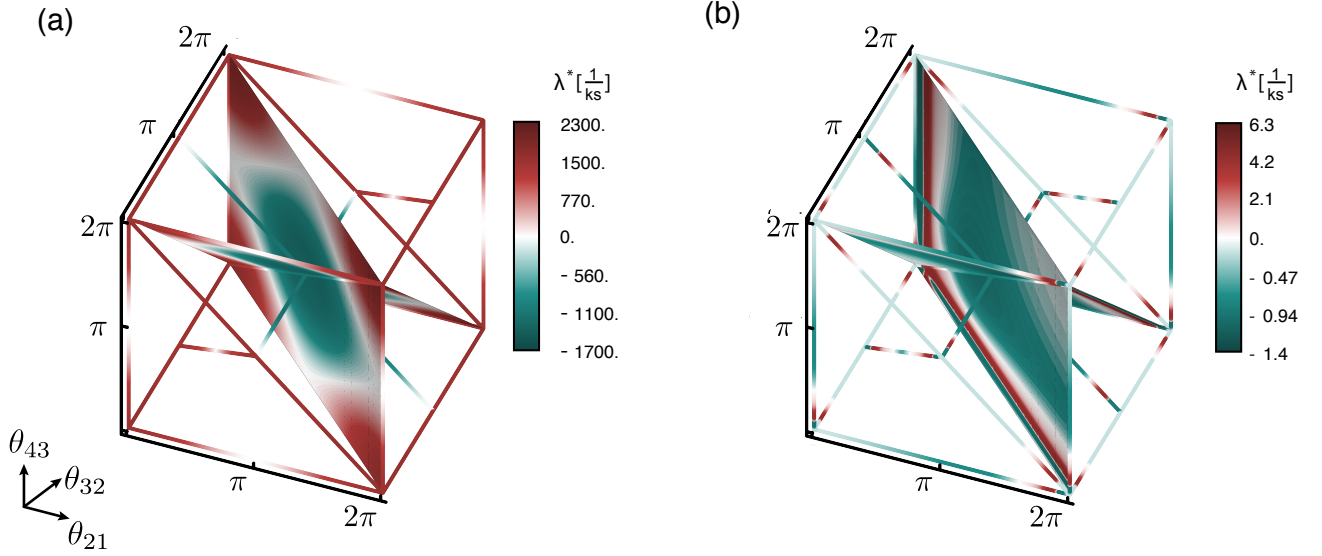
FIG. S7. **(a)** Maximum transverse eigenvalue of 4 ring of inhibitory Kuramoto oscillators invariant manifolds. The (D_1^s, D_1^s) and $(Z_2, 1)$ invariant manifolds are fully repelling. The (D_1^p, D_1^p) invariant manifolds are half repelling and half attracting. The $(D_1^s, 1)$ manifold is largely attracting. **(b)** Maximum transverse eigenvalue of best fit model of 4 ring of inhibitory BZ oscillators. All invariant manifolds are largely attracting, except $(Z_2, 1)$

are exclusively repelling except for $(D_1^s, 1)$ and (D_1^p, D_1^p) about Trot. The best fit BZ model's invariant manifolds are almost exclusively attracting, with the exception of $(Z_2, 1)$, which is half attracting and half repelling. These differences lead to distinct transient dynamics. While the BZ models will often form symmetric clusters on H/K-derived invariant manifolds before reaching steady-state, the Kuramoto model will not.

SV.   EULER CHARACTERISTIC OF A 3-TORUS

The Euler characteristic of a solid Polyhedra is given by:

$$\chi = V - E + F - C$$

which depends on integer number of vertices V, edges E, faces F, and number of 3D objects C. The 3-Torus is a cartesian cube with periodic boundary conditions. Thus it is a cubic polyhedra with very few unique vertices, edges, and faces.

Vertices: There are 8 vertices of a normal cube. If we consider any vertex at the edge of the periodic cube, we see they are related to one another by periodic boundary conditions, $V = 1$.

Edges: There are 12 edges of a normal cube. Each edge of the periodic cube is repeated 3 times. For example the edge $((0, 0, 0), (0, 0, 2\pi))$ is equal to $((2\pi, 0, 0), (2\pi, 0, 2\pi)), ((0, 0, 0), (0, 2\pi, 2\pi))$, and $((2\pi, 2\pi, 0), (2\pi, 2\pi, 2\pi))$. There are thus 3 unique edges, $E = 3$.

Faces: There are 6 faces to a normal cube. In the periodic cube each face is repeated twice, $F = 3$. Thus the Euler characteristic is 0: $\chi = 1 - 3 + 3 - 1 = 0$.